nature synthesis

Article

https://doi.org/10.1038/s44160-022-00234-x

Conversion of CO_2 to multicarbon products in strong acid by controlling the catalyst microenvironment

Received: 27 July 2022

Accepted: 16 December 2022

Published online: 09 February 2023

Check for updates

Yong Zhao[1,2,5], Long Hao[3,5], Adnan Ozden[1,5], Shijie Liu[1,5], Rui Kai Miao[1], Pengfei Ou[4], Tartela Alkayyali[1], Shuzhen Zhang[2], Jing Ning[3], Yongxiang Liang[4], Yi Xu[1], Mengyang Fan[1], Yuanjun Chen[4], Jianan Erick Huang[4], Ke Xie[4], Jinqiang Zhang[1,4], Colin P. O'Brien[1], Fengwang Li[2] ✉, Edward H. Sargent[4] & David Sinton[1] ✉

Electrosynthesis of multicarbon products from the reduction of CO_2 in acidic electrolytes is a promising approach to overcoming CO_2 reactant loss in alkaline and neutral electrolytes; however, the proton-rich environment near the catalyst surface favours the hydrogen evolution reaction, leading to low energy efficiency for multicarbon products. Here we report a heterogeneous catalyst adlayer—composed of covalent organic framework nanoparticles and cation-exchange ionomers—that suppresses hydrogen evolution and promotes CO_2-to-multicarbon conversion in strong acid. The imine and carbonyl-functionalized covalent organic framework regulates the ionomer structure, creating evenly distributed cation-carrying and hydrophilic–hydrophobic nanochannels that control the catalyst microenvironment. The resulting high local alkalinity and cation-enriched environment enables C–C coupling between 100 and 400 mA cm^{-2}. A multicarbon Faradaic efficiency of 75% is achieved at 200 mA cm^{-2}. The system demonstrates a full-cell multicarbon energy efficiency of 25%, which is a twofold improvement over the literature benchmark acidic system for the reduction of CO_2.

Electrocatalytic conversion of CO_2 provides a route to produce renewable, carbon-based chemical feedstocks and close anthropogenic carbon cycles[1,2]. Multicarbon ($C \geq 2$) products such as ethylene (C_2H_4) and ethanol (C_2H_5OH) are of particular interest due to their high market values and demand[3]. Despite recent advances in electrosynthesis of C_2 products[4–16], most systems rely on alkaline or neutral electrolytes to promote C–C coupling and suppress the competing hydrogen evolution reaction (HER)[17]. The local alkaline environment at the cathode–electrolyte interface induces carbonate formation, which leads to a low single pass CO_2 conversion efficiency (SPCE < 25% for C_2 products)[18]. Regenerating the lost CO_2 results in a substantial energy penalty that necessitates an additional 50% energy input to the alkaline CO_2 reduction (CO_2R) electrolysers[19–21]. In neutral electrolysers, carbonate crosses over to the anode, releasing CO_2, and the separation of CO_2 from the anodic O_2 stream incurs additional costs[22,23].

[1]Department of Mechanical and Industrial Engineering, University of Toronto, Toronto, Ontario, Canada. [2]School of Chemical and Biomolecular Engineering and The University of Sydney Nano Institute, University of Sydney, Sydney, New South Wales, Australia. [3]College of Chemistry and Pharmaceutical Sciences, Qingdao Agricultural University, Qingdao, China. [4]Department of Electrical and Computer Engineering, University of Toronto, Toronto, Ontario, Canada. [5]These authors contributed equally: Yong Zhao, Long Hao, Adnan Ozden, Shijie Liu. ✉e-mail: fengwang.li@sydney.edu.au; sinton@mie.utoronto.ca

Operating CO_2R in strongly acidic media (pH < 1) is one solution to address the CO_2 loss issue[24–28]. The locally alkaline environment required for multicarbon synthesis can be created by applying very high current densities (>1 A cm^{-2})[19]. The protons in the bulk acidic electrolyte convert locally formed carbonate back to CO_2 within the diffusion layer, preventing CO_2 cross-over to the anode; however, the high voltage (~4.2 V) required to drive such high current densities and the limited C_2 Faradaic efficiency (FE_{C_2}, ~48%) together result in a low energy efficiency (~12%)[19].

To improve energy efficiency, high C_2 selectivity at lower currents should be pursued, which would reduce Ohmic losses and the full cell voltage while maintaining sufficient reaction rates for industrial application (>100 mA cm^{-2})[29–32]; however, at moderate current densities (for example, 100–400 mA cm^{-2}), the influx of protons from the acidic surroundings (pH < 1) is greater than the local consumption of protons[24]. The resulting local environment (pH < 8) favours the HER and suppresses the formation of C_2 products[19]. Lowering the acidity of the bulk electrolyte (for example, to pH > 3) would improve local alkalinity yet comes at the cost of increased solution resistance (Supplementary Table 1) and a higher cell voltage.

We reasoned that a catalyst adlayer—to restrict proton influx at the catalyst–electrolyte interface—could improve the local alkalinity to a level that favours C_2 electrosynthesis (pH > 11) without sacrificing ion conductivity. The adlayer would need to selectively block proton transport from the diffusion layer (tens of micrometres thick) while increasing the concentration of metal ions (for example, K^+, Na^+, Cs^+) needed to promote the CO_2R (refs. [19,33,34]). Commercial cation-exchange thin films are adlayer candidates; however, the abundant cation-conducting hydrophilic domains in these films facilitate proton transport[35,36]. Incorporating organic nanofillers into the cation-exchange polymer matrix could potentially overcome this problem by breaking the proton-conducting networks while maintaining the accessibility of cations to the catalyst surface. As-formed heterogeneous thin layers could thereby exert independent control over both the local pH and the cation environment.

Here we report a heterogeneous cation-carrying, proton-blocking adlayer to enable efficient electrosynthesis of C_2 products on copper over a current density range of 100–400 mA cm^{-2} in acidic media (pH ≈ 1.0). We constructed the adlayer using insulating polymer nanoparticles (IPN) and a perfluorinated sulfonic-acid (PFSA) ionomer (Fig. 1a). We found that amphoteric covalent organic frameworks (COFs) with imine and carbonyl groups induced a uniform distribution of an oriented PFSA ionomer coating via electrostatic interactions. This composite structure confines proton transport to the hydrophilic nanochannels and enriches potassium ions near the catalyst surface. The regulated proton flux and cation distribution afforded the copper catalyst a kinetically favourable local environment for CO_2 activation (FE_{CO_2R} > 85%) and HER suppression (FE_{H_2} < 15%). This strategy enabled a C_2 Faradaic efficiency (FE) of 75% at 200 mA cm^{-2}. We demonstrated a system with a full-cell voltage of 3.5 V and an energy efficiency of 25% for acidic CO_2-to-C_2 conversion—double that of the literature benchmark[19].

Results and discussion

Modelling and experimental validation using the PS:PFSA adlayer

We began by modelling the proton-flux-constraining capability of a PFSA ionomer adlayer (5 µm thick) using a simplified three-dimensional ion transport model (simulating conditions at 200 mA cm^{-2} with an acidic boundary of 0.1 M protons; see Methods for details). In response to concentration gradients and electric fields, the protons (H^+) migrated to the catalyst surface and the produced hydroxide ions (OH^-) migrated to the bulk solution. The local pH was determined by the steady-state equilibrium between H^+, OH^- and H_2O according to the water-dissociation equilibrium. With the full ionomer layer, the catalyst surface reached a neutral pH (~7.6) at these conditions (Fig. 1b). When proton-insulating nanoparticles (500 nm in diameter) were embedded into the ionomer layer, proton transport was constrained further to the particle-interspaced ionomer nanochannels. The catalyst surface reached an alkalinity of pH ≈ 12.5 (Fig. 1c). Increasing the particle size or the layer thickness had little influence on the local alkalinity (Supplementary Fig. 1). Replacing the PFSA ionomer with water resulted in a substantial decrease of local alkalinity to pH ≈ 7.4 (Supplementary Fig. 1), demonstrating the efficacy of PFSA in limiting proton influx and outward hydroxide migration. The uniform distribution of PFSA ionomers in the adlayer is necessary to prevent acid penetration and realize high local alkalinity at the catalyst.

Seeking experimental evidence for the proton-flux-constraining design, we prepared a well-dispersed mixture of commercial polystyrene nanospheres (PS, 450 nm in diameter) and PFSA ionomers, and spray-coated the dispersion onto a 200 nm copper layer on a porous polytetrafluoroethylene (PTFE) substrate (Supplementary Figs. 2 and 3). A tightly packed adlayer (~5 µm thick) with PS:PFSA heterojunctions was formed with some isolated ionomer aggregates (Fig. 1d and Supplementary Fig. 4). An electrode with a full PFSA layer (~6 µm thick) was employed as the control (Supplementary Fig. 5). We investigated their apparent proton fluxes under various cathodic current densities using a permeation flow-cell (Fig. 1e). The OH^- produced from water dissociation was removed by the circulating water in the permeate chamber or was neutralized by the protons passed through the adlayer. The proton-flux-constraining effect was quantified by the change in pH of the permeate (Fig. 1f). The PS:PFSA adlayer efficiently limited proton flux towards the permeate, as evidenced by a high pH of >12 achieved after 6 min of electrolysis. By contrast, the PFSA-only layer realized only neutral conditions (pH ≈ 7). These observations are consistent with our modelling results. The apparent flux of protons through the PS:PSFA adlayer decreased by ~20% compared with the case with only a PSFA layer (Supplementary Fig. 6).

We then evaluated the CO_2R performance of the adlayer-modified PTFE–Cu electrodes in phosphoric acid solution (pH ≈ 1.0). Potassium ions (3 M) were added to the catholyte to facilitate multicarbon formation[19,33,34]. In the current density regime of 100–400 mA cm^{-2}, no CO_2R product was detected on the PFSA-modified electrode. Increasing the thickness of the PFSA adlayer to 11 µm enabled C_2H_4 production ($FE_{C_2H_4}$ < 10%) but H_2 evolution remained dominant (FE_{H_2} > 60%) (Supplementary Figs. 5 and 7). By contrast, the PS:PFSA-modified electrode suppressed the competing HER (FE_{H_2} ≈ 40%) and achieved productive CO_2-to-C_2 conversion (Fig. 1g). Increasing the adlayer thickness impaired C_2 formation (Supplementary Fig. 8). The peak $FE_{C_2H_4}$ and FE_{C_2} values at 250 mA cm^{-2} are 23% and 43%, respectively, which are comparable with the best results (28% and 48%) previously achieved at a similar electrolyte pH and much high current densities (~1,200 mA cm^{-2})[19]. The deposition of copper nanoparticles on the previously reported[19] electrically conductive adlayer during CO_2R facilitates the HER (Supplementary Fig. 9), confirming the need for insulating material within the adlayer.

Although the PS:PFSA adlayer structure shows promise for C_2 electrosynthesis at moderate current densities, the prevailing HER (FE_{H_2} ≈ 40%) precludes energy-efficient CO_2-to-C_2 conversion in strong acid. When PFSA—an ionomer with a hydrophobic fluorocarbon (–CF_2–) backbone and hydrophilic sulfonic-acid group (–SO_3H)-terminated side chains—is mixed with hydrophobic polystyrene, it is unevenly distributed among polystyrene nanospheres due to their weak interactions[36,37]. With an uneven distribution of cation-carrying nanochannels (Supplementary Figs. 4 and 10), regions of high local acid penetration allowed the HER to dominate the overall reaction. The disordered PFSA configuration also blocked the diffusion of locally produced anions (HCO_3^- or CO_3^{2-}) and gases (CO_2R products or regenerated CO_2), resulting in carbonate deposition and ionomer aggregation/migration in the adlayer (Supplementary Fig. 11), and a short lifetime (Supplementary Fig. 12). Similar effects on local ion or gas transport

https://doi.org/10.1038/s44160-022-00234-x

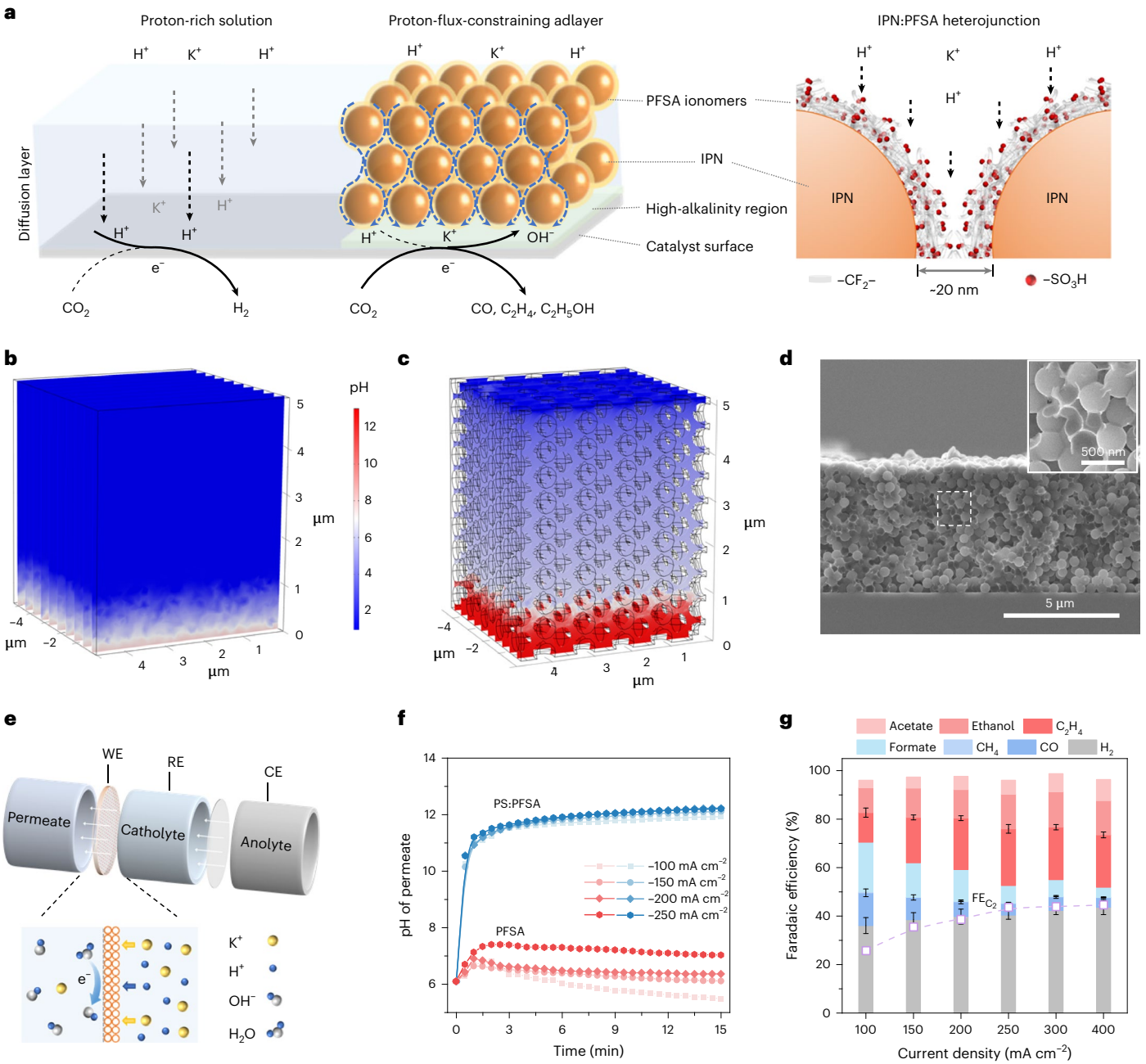

Fig. 1 | Catalyst microenvironment control in acidic media via proton-flux-constraining ionomer adlayer design. a, Schematics of interfacial reactions and proton transport near catalyst surface. **b**,**c** Modelled pH profiles for the 5 μm PFSA layer (**b**) and 5 μm IPN:PFSA adlayer (**c**) over a 200-nm-thick catalyst. The nanofillers in **c** were omitted. **d**, Cross-sectional SEM image of a PS:PFSA adlayer on silicon substrate. Inset shows a magnified SEM image of the square region highlighted by the white dashed lines. A thin carbon layer was sputtered onto the surface to eliminate charging and outline the ionomer structure. **e**, Schematic illustration of the experimental set-up for ion flux measurements. WE, working electrode; CE, counter electrode; RE, reference electrode. **f**, The pH change of permeate during 15 min of electrolysis at cathodic current densities of 100–250 mA cm^{-2} for PS:PFSA- and PFSA-modified electrodes. **g**, CO_2R product distribution of PS:PFSA-modified PTFE–Cu electrodes. Values are means and error bars indicate s.d. ($n = 3$ replicates). The hollow squares indicate FE_{C_2}.

due to uneven ionomer distribution are well established in the field of proton exchange membrane fuel cells[38–40].

COF:PFSA adlayer for efficient C_2 electrosynthesis

We sought to design an ordered adlayer to suppress the HER and steer C_2 electrosynthesis (Fig. 2). We expected that a more uniform distribution of strongly bound ionomers would be formed on positively charged hydrophilic nanoparticles with a highly uniform surface chemistry. A locally ordered PFSA configuration with alternating layers of $-SO_3H$-rich and $-CF_2$-rich domains could be formed at the heterojunction (Fig. 2a)[36,37]. In this scenario, cation (hydrated H^+ and K^+) transport is confined to the hydrophilic laminar nanochannels, whereas the locally produced gases can diffuse out via the oriented hydrophobic channels—preventing blistering of the adlayer that would allow acid penetration. Potassium ions have a higher affinity for the sulfonate groups ($-SO_3^-$) than H^+ (ref. [36]), and thus they can be trapped and stabilized in the hydrophilic nanochannels to reduce cation transport. Such an adlayer would enable regulation of the proton flux over all catalytic sites, with ionomer-stabilized K^+ ions near the catalyst surface for CO_2 activation and reduction.

https://doi.org/10.1038/s44160-022-00234-x

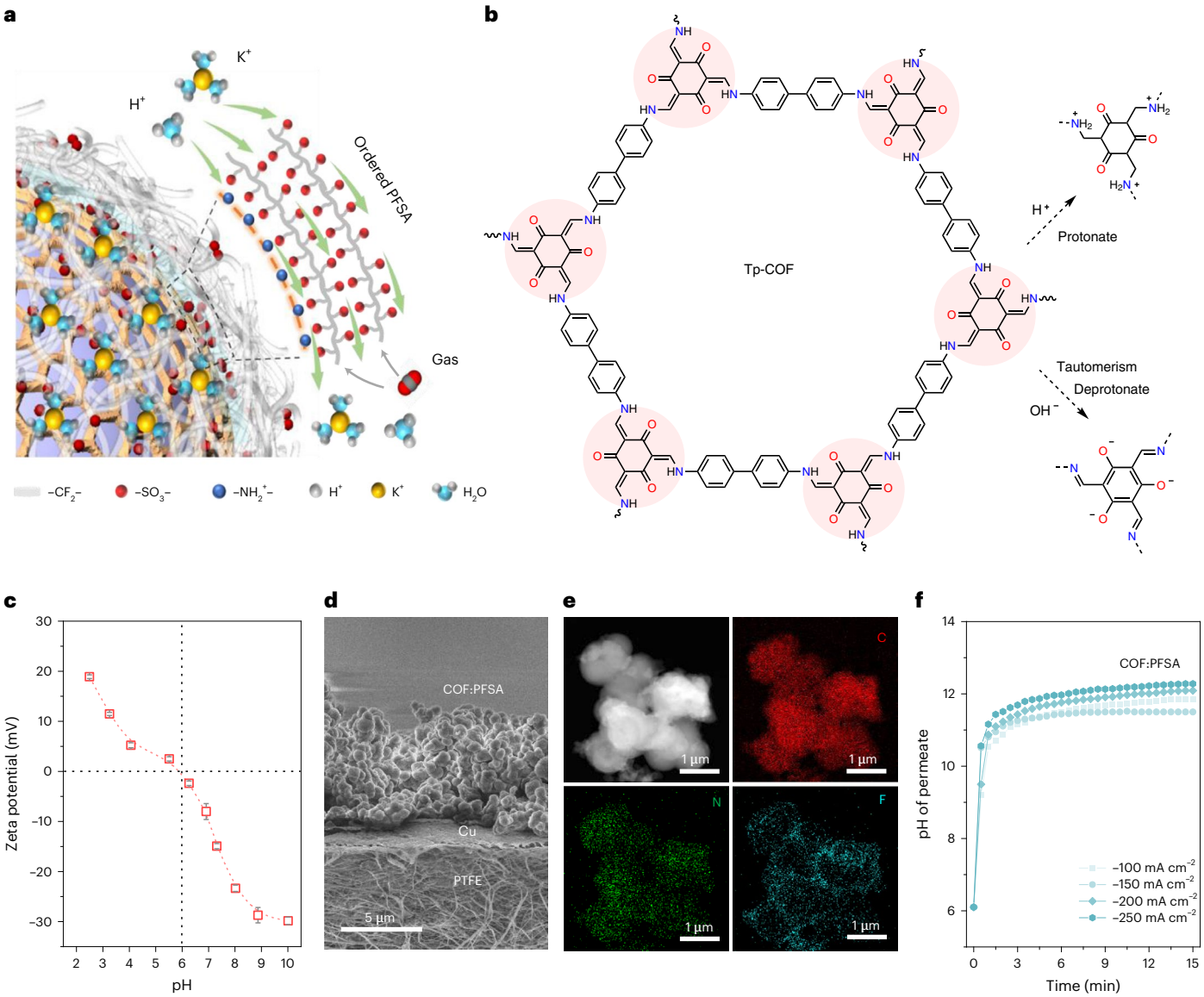

Fig. 2 | Structure and proton-flux-constraining property of COF:PFSA heterojunction. a, Schematic illustration of a functionalized COF particle for regulating ionomer structure and local ions and gas transport. Laminar PFSA ionomer arrangements have been reported depending on the thickness and substrate[36]. **b**, Structure of amphoteric Tp-COF and its sensitivity to the surrounding acidity. The red shadings indicate the functional groups of the Tp-COF. **c**, Zeta potentials of nanoparticles-assembled COF membranes in 5 mM KCl solution at pH 2–10. Values are means and error bars indicate s.d. ($n = 3$ replicates). **d**, Cross-sectional SEM image of COF:PFSA adlayer on PTFE–Cu substrate. **e**, TEM-EDS mapping of COF:PFSA composite. **f**, The pH change of permeate during 15 min of electrolysis at cathodic current densities of 100–250 mA cm^{-2} for COF:PFSA-adlayer-modified electrodes in a permeation cell.

Noting that nitrogen sites could introduce positive surface charges and improve the ionomer distribution on the substrate[38,40], we substituted the bare polystyrene with nitrogen-containing polystyrene nanospheres that were positively charged in acidic conditions (Supplementary Fig. 13). The formed adlayer exhibited greater HER suppression ($FE_{H_2} \approx 20–30\%$) than the bare polystyrene counterpart ($FE_{H_2} \approx 40\%$) (Supplementary Fig. 14); however, the C_2 selectivity achieved in this configuration was low (<48%), as was the stability (<1 h)—an outcome we attribute to unevenly distributed nitrogen sites and a disordered PFSA ionomer adlayer (Supplementary Fig. 15).

To overcome this problem, we turned our attention to COFs, a class of crystalline porous polymers which combines hydrophilicity, uniformity and precisely tunable surface function[41–43]. We reasoned that the COF nanoparticles with a reticular imine group distribution would simultaneously regulate the dispersity and molecular configuration of PFSA ionomers, forming an efficient proton-flux-constraining adlayer. Noting the critical role of cations (for example, K^+, Na^+, Cs^+) in enabling CO_2R in acidic conditions[19,33,34], we sought additional cation-adsorption sites on the COF to promote the cation enrichment approximate to the catalyst surface.

To implement this strategy experimentally, we synthesized an acid-resistant triformylphloroglucinol and benzidine-derived amphoteric COF (Tp-COF, where Tp is 1,3,5-triformylphloroglucinol) rich in imine and carbonyl groups (Fig. 2b and Supplementary Fig. 16). The imine groups are protonated to form positively charged sites in acidic solution (pH < 6) (Fig. 2b,c), which can interact with the $-SO_3^-$ groups of PFSA to increase its adhesion to the COF and regulate its microstructure. The electron-rich carbonyl groups create a negatively charged COF surface under neutral and alkaline conditions (pH > 6) via tautomerism and deprotonation (Fig. 2b,c and Supplementary

https://doi.org/10.1038/s44160-022-00234-x

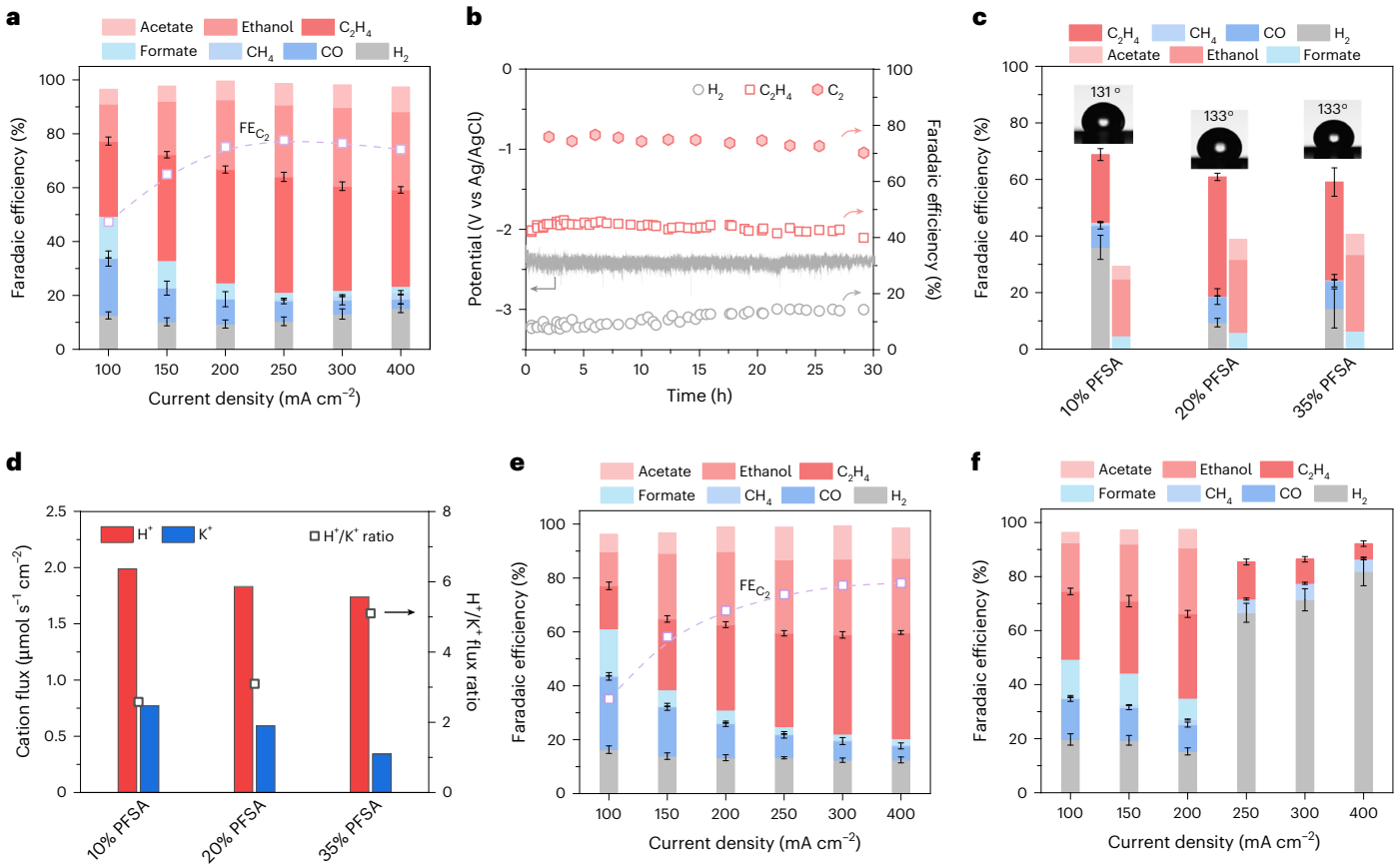

Fig. 3 | COF:PFSA adlayer enables efficient multicarbon electrosynthesis on copper in acidic electrolyte. a, CO_2R product distribution of COF:PFSA-modified PTFE–Cu electrodes in phosphate solution with 3 M KCl (pH ≈ 1.0). Values are means and error bars indicate s.d. ($n = 3$ replicates). The hollow squares indicate FE_{C_2}. **b**, An extended CO_2R operation and product distribution of COF:PFSA-modified PTFE–Cu electrode in a three-electrode flow-cell. **c**, Influence of the PFSA ionomer content in the Tp-COF adlayer on CO_2R product distribution. The insets show the corresponding static contact angles. Values are means and error bars indicate s.d. ($n = 3$ replicates). **d**, The apparent cation fluxes passing through various COF:PFSA adlayers, and the corresponding H^+/K^+ flux ratios at 200 mA cm^{-2}. **e**,**f**, CO_2R product distribution of Tf-COF:PFSA-modified (**e**) and COF:Aemion-modified (**f**) PTFE–Cu electrodes in phosphate solution (3 M KCl, pH ≈ 1.0). Values are means and error bars indicate s.d. ($n = 3$ replicates). The hollow squares indicate FE_{C_2}.

Fig. 17), which could facilitate K^+ stabilization near catalyst and CO_2R kinetics[44,45]. Scanning electron microscopy (SEM) images revealed a homogeneous porous nanoparticle-assembled COF:PFSA adlayer (~10 μm thick) over the PTFE-supported copper catalyst layer (Fig. 2d). Transmission electron microscopy (TEM) energy-dispersive X-ray spectroscopy (EDS) mapping revealed an even ionomer distribution on the COF particles (Fig. 2e). The ionomer thickness was estimated to be around 10 nm (Supplementary Fig. 18), which is equivalent to ~20 layers of ordered PFSA molecules (side chain length ≈ 0.5 nm) in which $-SO_3^-$ groups tend to face the COF surface[10,46,47]. The COF:PFSA adlayer exhibited excellent proton-flux-constraining capability at each applied current density (Fig. 2f).

We examined the CO_2R performance of the COF:PFSA-adlayer-modified copper electrodes in the same acidic conditions as employed in the PS:PFSA case. Over the full current density range (100–400 mA cm^{-2}), the COF:PFSA adlayer greatly suppressed the competing HER (<15%) and improved CO_2R selectivity (FE > 85%) (Fig. 3a). The FE_{C_2} values showed a volcano trend with a peak of 78% at 250 mA cm^{-2}. At 200 mA cm^{-2}, FE_{H_2} was suppressed to 9% and FE_{C_2} reached 75% (42% towards C_2H_4, 26% towards C_2H_5OH and 7% towards CH_3COOH) with a C_2 partial current density of 150 mA cm^{-2} (Supplementary Fig. 19). The value of FE_{C_2} remained nearly constant as the electrolyte acidity was reduced from pH 0.7 to 1.9 (Supplementary Fig. 20), whereas FE decreased with decreasing K^+ concentration from 3 M to 0.5 M (Supplementary Fig. 21). A sufficient concentration of K^+ ions (at least 2 M) is essential for efficient C_2 production. Increasing the COF:PFSA-adlayer thickness from 10 μm to 19 μm caused the HER to increase from 9% to 17% and FE_{C_2} to decrease from 75% to 69% (Supplementary Fig. 22). The increased COF layer thickness creates a more effective proton transport barrier but simultaneously prevents K^+ access. The lack or absence of K^+ near the catalyst intensifies H_2 production and suppresses CO_2R (Supplementary Fig. 21). No obvious interaction between the nitrogen-rich COF and copper surface was detected to contribute to C_2 formation (Supplementary Fig. 23). The crystallinity and specific surface area of COF nanoparticles did not impact the catalytic performance (Supplementary Fig. 24). In an extended electrolysis at 200 mA cm^{-2}, the reaction maintained an FE_{C_2} of 75% for 20 h, and was still at >70% after 30 h of electrolysis (Fig. 3b). Scanning electron microscopy and TEM-EDS analyses revealed a well-maintained adlayer macrostructure and COF:PFSA heterogeneous microstructure after the extended electrolysis (Supplementary Figs. 25 and 26). We attribute the performance degradation after 20 h to the gradual flooding of hydrophobic domains by the liquid CO_2R products (for example, C_2H_5OH), allowing increased proton flux (Supplementary Fig. 27).

Decoupling the impacts of COF:PFSA adlayer on C_2 production

The FE_{C_2} and stability surpass the best results obtained in previous acidic systems[19], and are comparable with those of alkaline and neutral systems using state-of-the-art catalysts[6,7,12,16,48,49]. This suggests that the COF:PFSA is able to create a robust, favourable alkaline and

https://doi.org/10.1038/s44160-022-00234-x

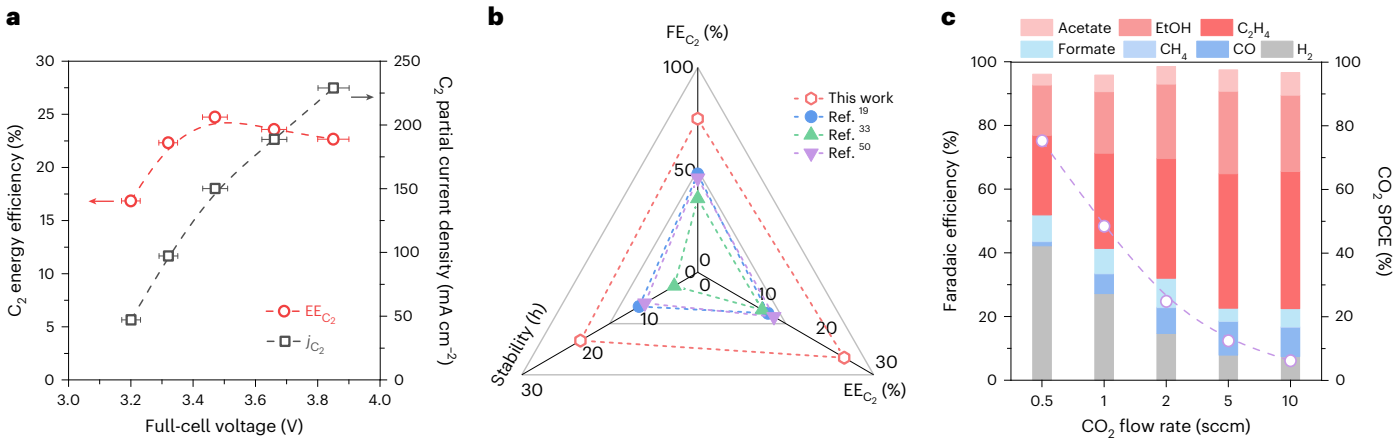

Fig. 4 | Acidic CO_2-to-multicarbon electrosynthesis in a slim flow-cell. **a,** Full-cell voltage, energy efficiency and partial current density for C_2 formation. The full-cell voltages are presented without iR compensation. Values are means and error bars indicate s.d. ($n = 3$ replicates). **b**, Comparison of C_2 FE, energy efficiency and stability of a COF:PFSA-modified PTFE–Cu electrode with those of previously reported acidic CO_2R systems. Comparisons are constrained to reports with C_2 production. **c**, CO_2R product distribution (column data) and SPCE (circle data) of CO_2 to all products on a COF:PFSA-modified PTFE–Cu electrode at various CO_2 flow rates at 200 mA cm^{-2}.

K^+-enriched microenvironment near the catalyst for stable CO_2-to-C_2 conversion. Specifically, the COF-enabled uniform ionomer distribution and ordered hydrophilic nanochannels regulate the proton flux and improve the local pH over all catalytic sites, whereas the ionomer-stabilized K^+ ions proximate to these active sites promote the kinetics of CO_2R under proton-depleted local conditions. The ordered hydrophobic domains facilitate the diffusion of locally produced gas and prevent the accumulated microbubbles from breaking the adlayer, thereby offering a mechanically stable environment for ion transport and interfacial reactions.

However, constraining the proton flux to improve local pH also blocks K^+ ions due to their shared cationic identities and transport pathways. We posited that a microenvironment that is both alkaline and K^+-rich is achieved by tuning the cation-flux-constraining capability of the COF:PFSA adlayer.

To test this hypothesis, we varied the density of cation-carrying nanochannels by tuning the ionomer content in the COF:PFSA adlayer (Fig. 3c and Supplementary Fig. 28). Decreasing the PFSA content from 20 wt% to 10 wt% experimentally did not affect the hydrophobicity of the adlayer (contact angle ≈ 131°) but led to a gradual increase in FE_{H_2} from 9% to 36%, accompanied by a reduced FE_{C_2} from 75% to 49% at 200 mA cm^{-2}. Ion permeation measurements confirmed that the lower ionomer content adlayer permitted a higher proton flux (Fig. 3d). The high sensitivity of CO_2R to the local proton concentration was further verified by reducing the density of $-SO_3H$ groups in the adlayer (20 wt% case). Replacing the used ionomer (equivalent weight (EW) = 790 g mol^{-1} SO_3H) with a higher-EW ionomer (1,100 g mol^{-1} SO_3H) caused a substantial increase in FE_{H_2} at various current densities (Supplementary Fig. 29)—a trend nearly identical to the 10 wt% and 13 wt% cases (Supplementary Fig. 28).

Increasing the ionomer content from 20 wt% to 35 wt% slightly improved the proton-flux-constraining capability compared with the 20 wt% case; however, FE_{H_2} also increased from 9% to 14% and $FE_{C_2H_4}$ decreased from 42% to 35% (Fig. 3c). Ion permeation measurements revealed that K^+ transport was more affected than H^+ transport by the ionomer content, especially at higher ionomer loadings, as reflected by the increased H^+/K^+ flux ratio from 2.4 (10 wt%) to 3.1 (20 wt%) and further to 5.1 (35 wt%) (Fig. 3d). The difference is attributed to the larger ionic size of K^+ and its higher affinity to $-SO_3^-$. The K^+ transport flux measured in the permeation cell demonstrated the cation-enrichment effect achieved in the adlayer: 35 wt% case < 20 wt% case.

The COF surface may also contribute to K^+ enrichment via its nucleophilic carbonyl groups. To assess the impact of the carbonyl groups, we employed a solely imine-containing Tf-COF (where Tf is 1,3,5-triformylbenzene) as the control (Supplementary Fig. 30). The synthesized Tf-COF resembles Tp-COF in microstructure and enables the formation of uniform heterojunctions (Supplementary Fig. 31). The formed adlayer exhibited nearly identical proton-flux-constraining behaviours to the Tp-COF adlayer (Supplementary Fig. 32), suggesting that they possess a similar capacity to create a locally alkaline environment; however, the Tf-COF-adlayer-modified electrode exhibited higher FE_{H_2} and lower FE_{C_2} values than the Tp-COF counterpart at current densities lower than 250 mA cm^{-2} (Fig. 3e and Supplementary Fig. 33). At 200 mA cm^{-2}, FE_{H_2} increased from 9% to 13%, whereas FE_{C_2} decreased from 75% to 68%. The crystallinity and specific surface area of Tf-COF particles did not impact the catalytic performance (Supplementary Fig. 34). We attributed the higher FE_{C_2} of the Tp-COF case to its carbonyl groups. This trend agrees with the density function theory (DFT) prediction that the Tp-COF adlayer absorbs K^+ more strongly than Tf-COF (Supplementary Fig. 35). These sites could localize K^+ in the water layers near the Tp-COF surface, leading to a higher local K^+ concentration in the vicinity of catalyst, as verified by depth-profiling X-ray photoelectron spectroscopy analysis (Supplementary Fig. 36). We further investigated the impact of the local K^+ concentration on CO_2R by analysing the C–C coupling step towards C_2 formation (that is, *CO + *CO → *OCCO; Supplementary Fig. 35). The DFT results indicate that a higher local K^+ concentration promotes C–C coupling thermodynamically and kinetically, probably via the induced solvation effect and electrostatic field enhancement[33,34], steering the CO_2R towards C_2 products.

To assess the role of the ordered PFSA hydrophobic domains, we employed Aemion—an anion exchange ionomer with hydrophilic backbones—as the control (Supplementary Fig. 37). The COF:Aemion-20wt% adlayer exhibited a proton-flux-constraining capability comparable with the COF:PFSA adlayer at 200 mA cm^{-2} (Supplementary Fig. 38). The Aemion ionomer decreases the concentration of K^+ ions near the catalyst (H^+/K^+ flux ratio of ~14) due to Donnan exclusion. The structural cation centres on the ionomer can replace K^+ for CO_2 activation[50]. This adlayer-modified electrode exhibited a suppressed HER ($FE_{H_2} \approx 15\%$) and considerable C_2 formation ($FE_{C_2} \approx 63\%$) at 200 mA cm^{-2} (Fig. 3f); however, the adlayer was quickly blistered and broken by the accumulated gas due to the lack of gas-diffusion nanochannels, which limited

the catalytic stability to less than 1 h (Supplementary Fig. 39). At higher current densities (>200 mA cm^{-2}), the hydrophilic adlayer cannot constrain the proton flux efficiently, as verified by the dominant HER (FE_{H_2} > 70%). These results indicate the importance of the gas transport and proton-flux regulation enabled by the ordered hydrophobic domains within the COF:PFSA adlayer.

Energy efficiency and carbon efficiency towards C_2 products

To assess the energy efficiency towards C_2 products, we operated the COF:PFSA-adlayer-modified copper electrodes in a low-resistance slim flow-cell at moderate current densities of 100–300 mA cm^{-2} (Supplementary Fig. 40). The CO_2R product distribution was nearly identical to that obtained in the half-cell measurements. Within this regime, we achieved a CO_2R FE of >85%, which is comparable with the selectivity of the literature benchmark neutral and alkaline-media CO_2R systems[8,10,51]. The full-cell voltage was in the range of −3.2 to −3.9 V (with no compensation for solution resistance), and the derived EE_{C_2} exhibited a volcano trend with a maximum of 25% at −3.47 V with a C_2 partial current density of 150 mA cm^{-2} (Fig. 4a). We operated the full-cell electrolysis at this condition for an initial 10 h test (Supplementary Fig. 41). The FE_{C_2} value was maintained at ~75% and the full-cell voltage at around −3.5 V, suggesting a stable EE_{C_2} value of ~25% for C_2 production in this system. This C_2 energy efficiency represents a twofold improvement over the literature benchmark acidic CO_2R system (Fig. 4b and Supplementary Table 2)[19].

We assessed the capability of the COF:PFSA-modified PTFE–Cu electrode on SPCE by constraining the availability of CO_2 (Fig. 4c). Upon reducing the flow rate of CO_2 from 10 to 0.5 standard cubic centimetres per minute (sccm), the SPCE increased from 6% to 75% for all CO_2R products at 200 mA cm^{-2}. The SPCE for C_2 products was 45% at 0.5 sccm, surpassing the theoretical limit of 25% in alkaline systems and comparable to the literature benchmark of 50% in acidic systems[19,50].

Conclusion

The heterogeneous ionomer coating enables control of the catalyst microenvironment and thereby efficient C_2 electrosynthesis in strongly acidic media. This strategy is applicable to other catalysts and current density regimes (Supplementary Fig. 42). The approach provides a route to achieve a kinetically favourable local environment for C–C coupling without requiring high operating current densities and voltages. It thus offers a pathway to improve the energy efficiency and operational stability for CO_2-to-C_2 conversion in acidic media. We demonstrated C_2 production metrics (75% FE, 25% energy efficiency, and 20 h stability at 200 mA cm^{-2}) that are competitive with the conventional alkaline and neutral CO_2R flow-cell systems using standard copper catalysts. The CO_2 single pass conversion achieved (45% towards C_2 products) surpasses the fundamental limit of alkaline systems. This approach offers a solution to the challenge of reactant loss that has limited the field of CO_2 electroreduction.

Methods

Chemicals and materials

The chemicals used for electrolytes and electrode preparation, including phosphoric acid (85%), potassium chloride, potassium hydroxide, sulfuric acid (98%), PFSA (Aquivion, D79-25BS, EW = 760 g mol^{-1}), PFSA (Nafion, EW = 1,100 g mol^{-1}), copper nanoparticles (25 nm), carbon nanoparticles and nitrogen-containing polystyrene nanospheres (460 nm) were purchased from Sigma-Aldrich. The chemicals used for COF synthesis, including 1,3,5-triformylbenzene, 3,5-triformylphloroglucinol, benzidine, pyrrolidine, *ortho*-dichlorobenzene, *n*-butyl alcohol, 1,3,5-benzenetriboronic acid, 1,4-dioxane, mesitylene and *N*,*N*-dimethylformamide, were purchased from Energy Chemical. The non-functionalized polystyrene microspheres (450 nm) were purchased from Alpha Nanotech. The anion-exchange ionomer powder (Aemion, AP1-CNN5-00-X) was purchased from Ionomr Innovations. The Nafion 117 membrane and platinum mesh (grid aperture of 0.98 × 1.4 mm; purity 99.95%) were purchased from Fuel Cell Store. The PTFE gas diffusion layer (pore size = 450 nm) was purchased from the Beijing Zhongxingweiye Instrument Company. Deionized water (18.2 MΩ) was used for the preparation of all electrolytes.

Synthesis of COFs

Tp-COF and Tf-COF were prepared according to past reports, with modifications[52–54]. For the synthesis of Tp-COF[52], Tp (84.1 mg), benzidine (110.5 mg), pyrrolidine (Py, 0.5 ml), *ortho*-dichlorobenzene (*o*-DCB, 4.5 ml) and *n*-butyl alcohol (*n*-BuOH, 0.5 ml) were mixed in a pyrex tube (80 ml). The mixture was sonicated for 10 min, degassed through three freeze–pump–thaw cycles, sealed under vacuum and heated at 120 °C for 72 h. After cooling to room temperature, the precipitate was centrifuged, washed with tetrahydrofuran and dried in the vacuum oven at 60 °C overnight to obtain Tp-COF powders with high crystallinity. To synthesize Tp-COF with low crystallinity, the volume of Py, *o*-DCB and *n*-BuOH was changed to 0.1 ml, 2.5 ml and 2.5 ml, respectively.

For the synthesis of Tf-COF[53], Tf (64.8 mg), benzidine (110.5 mg), 1,4-dioxane (2 ml) and mesitylene (2 ml) were mixed in a 25 ml pyrex tube. After sonication, acetic acid (0.4 ml, 6 M) was added into the tube. The same conditions were used to produce Tf-COF powders with high crystallinity. To synthesize poorly crystalline Tf-COF[54], Tf (64.8 mg) and benzidine (110.5 mg) were dissolved into acetonitrile (50 ml) in a glass bottle. After adding acetic acid solution (4 ml, 12 M), the reactor was allowed to stand at room temperature for 72 h. The precipitate was collected, washed and dried to obtain Tf-COF powders with low crystallinity.

Characterization

Scanning electron microscopy imaging was performed using a scanning electron microscope (FEI Quanta FEG 250). Transmission electron microscopy imaging and EDS analysis were performed on JEOL JEM-F200 and JEOL ARM-200F field-emission transmission electron microscopes operating at a 200 kV accelerating voltage, respectively. Contact angles were conducted using water droplets via Attension Theta (Biolin Scientific). X-ray diffraction data were collected on a D8 Advance diffractometer in reflection geometry operating with a copper Kα anode (λ = 1.54178 Å) at 40 kV and 40 mA, and with a slit width of 0.1 mm. X-ray photoelectron spectroscopy measurements were performed on a device (PHI 5700) with aluminium Kα X-ray energy source (1486.6 eV) for excitation. Nitrogen adsorption/desorption isotherm measurements at 77 K were performed with an ASAP 2020 plus HD88 analyser, and the Brunauer–Emmett–Teller method and density functional theory pore model were used to calculate the specific surface areas and pore size distributions, respectively.

Electrode preparation

The bare PTFE–Cu electrodes were prepared by sputtering pure copper (>99.99%) onto PTFE substrates in the vacuum environment (~10^{-5}–10^{-6} Torr) of an Angstrom Nexdep system. The deposition rate was kept constant at 1 Å s^{-1} and the thickness of copper catalyst layer was 200 nm. Adlayer-modified PTFE–Cu electrodes were prepared by spray-coating a nanoparticles/ionomers methanol dispersion (solid concentration of ~0.6 mg ml^{-1}) onto the as-prepared PTFE–Cu substrates on a 50 °C hotplate. A proper mask was used to preserve the edge part of each PTFE–Cu substrate for electricity conducting (Supplementary Fig. 3). Without specifications, the nominal loading of polymer nanoparticles (that is, PS, Tp-COF or Tf-COF) was 1.0 mg cm^{-2}, and the weight ratio (wt%) of ionomers in the dispersion was 20%.

Flow-cell assembly

The flow-cell set-up consists of three compartments: the anolyte, catholyte and gas-flow chambers. The geometric area of the electrode

window was 1 × 1 cm^2. The cathode was clamped between the catholyte and gas-flow chambers, with the catalyst side facing the catholyte. A platinum gauze was employed as the anode, and an Ag/AgCl electrode (3 M KCl, CHI instrument) was used as the reference electrode in catholyte chamber. The catholyte and anolyte chambers were separated by a Nafion membrane. The catholyte and anolyte were circulated by peristaltic pumps at a constant rate of ~10 ml min^{-1}. A digital mass flow controller (SmartTrack 100, Sierra) was used to control the CO_2 flow rate in the gas flow chamber. The CO_2 and N_2 gas cylinders were purchased from Linde Gas.

Full-cell measurements were performed in a slim flow-cell set-up with a configuration similar to the above-mentioned flow-cell. The three chambers were designed to ensure a proximity between the cathode and anode to minimize the Ohmic losses. When assembled, the distance between the cathode and anode electrode is ~1 mm. In the full-cell system, we paired CO_2R cathode with an oxygen evolution reaction anode, that is, a titanium felt supported iridium oxide (IrO_x–Ti) electrode. The mass loading of the IrO_x catalyst was ~2.0 mg cm^{-2}.

Electrochemical measurement

All of the electrochemical tests were performed using an electrochemical workstation (Autolab PGSTAT302N) connected to a current booster (Metrohm Autolab, 10 A). The catholytes of pH 0.7, 1.0, 1.3 or 1.9 were prepared by introducing a specific amount of KOH into 1 M phosphoric acid solution. The K^+ concentration for each solution was adjusted to 3 M using KCl. The CO_2R performance was tested in a flow-cell assembly under galvanostatic mode. The phosphate solution was used as catholyte, and 0.5 M sulfuric acid was used as anolyte. The PTFE–Cu or adlayer-modified PTFE–Cu electrode was used as the cathode. The volumes of catholyte and anolyte used for circulation were 20 ml. The current densities reported are based on geometric surface area.

CO_2R product analysis

The gas products were collected from the gas outlet of the flow-cell and injected into a gas chromatograph (PerkinElmer Clarus 680) for gas quantification. The gas chromatograph was equipped with a thermal conductivity detector for the detection of H_2, O_2, N_2 and CO signals and a flame ionization detector for the detection of CH_4 and C_2H_4 signals. The gas chromatograph was composed of packed columns of molecular sieves (5 Å) and Carboxen-1000, and employed Argon (Linde, 99.999%) as the carrier gas. The liquid products were analysed using ^1H NMR spectroscopy (600 MHz Agilent DD2 NMR Spectrometer) with water suppression. Dimethyl sulfoxide was used as the reference standard and deuterium oxide as the lock solvent. The FE was calculated using the equations:

$$FE_{gas} = \frac{z \times F \times v \times r}{j \times V_m} \text{ and } FE_{liquid} = \frac{z \times F \times n_{product}}{Q}$$

where z is the number of electrons transferred, F is Faraday's constant (96,485 C mol^{-1}), v is the gas flow rate at the outlet of gas chamber (l min^{-1}), r is the concentration of detected gas product in parts per million, j is the total current (A), V_m is the unit molar volume of gas (24.5 l mol^{-1}), $n_{product}$ is the total moles of product derived from NMR analysis, and Q is the total charge (C).

The CO_2 SPCE towards each product was determined using the following equation at 25 °C, 1 atm:

$$SPCE = \frac{(j_{product} \times 60\,s)/(n \times F)}{(v \times 1\,min)/V_m}$$

where $j_{product}$ is the partial current (A) of a specific CO_2R product, and n is the electron transfer for the formation of each product molecule and V_m = 24.5 l mol^{-1}.

The full-cell energy efficiency for each product was calculated as follows:

$$EE_{product} = \frac{\left(1.23 + \left(-E^0_{product}\right)\right) \times FE_{product}}{-E_{cell}}$$

where $E^0_{product}$ is the thermodynamic potential for the formation of a specific CO_2R product, $FE_{product}$ is the calculated FE of the product and E_{cell} is the full-cell voltage without Ohmic loss correction evaluated in the slim flow cell.

Ion permeation measurement

The ion fluxes passing through various adlayers were evaluated using a permeation flow-cell consisting of a permeate chamber, a catholyte chamber and an anolyte chamber, with a cross-sectional chamber area of 1 × 1 cm^2. Hydrophilic PTFE substrates with similar porosity to the hydrophobic ones were used to prepare various adlayer-modified PTFE–Cu electrodes for the ion permeation tests. The hydrophilic PTFE–Cu/adlayer working electrodes were clamped between the permeate and catholyte chambers, with the adlayer-facing catholyte. A platinum gauze was used as the anode and an Ag/AgCl (3 M KCl) electrode was used as the reference electrode. The catholyte and anolyte chambers were separated by a piece of Nafion film.

Deionized water (30 ml), phosphate solution (containing 3 M KCl, pH ≈ 1.0) and 0.5 M H_2SO_4 were circulated at a constant rate of 50 ml min^{-1} in the permeate, catholyte and anolyte chambers, respectively. The deionized water in the permeate reservoir was purged with argon for 30 min to remove the oxygen inside. To drive ion migration, a cathodic current was applied to the working electrode, in which only the water reduction reaction occurred ($H_2O + 2e^- \rightarrow H_2 + 2OH^-$) on the surface of copper catalyst. Electrolysis was performed for 15 min, during which the pH value in the permeate reservoir was monitored by a calibrated pH meter. The K^+ concentration in the permeate reservoir was analysed by inductively coupled plasma (ICP) after the reaction. The apparent H^+ and K^+ fluxes were calculated respectively:

$$\text{Flux}\,(H^+) = \frac{(I \times t)/(z \times F) - V \times 10^{pH-14}}{t \times A} \text{ and flux}\,(K^+) = \frac{c \times V}{t \times A}$$

where I is the current applied on the working electrode (A), t is the reaction time (s), z is the number of electrons transferred for each OH^- ion produced, V is the volume of deionized water in the permeate reservoir (l), A is the cross-sectional area of the permeation window (cm^2), and c is the concentration of K^+ measured by ICP (mol l^{-1}).

Three-dimensional COMSOL simulation

The three-dimensional ion mass transport over the catalyst surface was modelled by COMSOL Multiphysics (v.5.5). The Secondary Current Distribution and Transport of Diluted Species physics interfaces were used to model the distribution and transport of H^+, OH^- and H_2O near the electrode. To mimic the heterogeneous IPN:PFSA adlayer, a hexagonal close-packed nanosphere assembly was generated in SOLIDWORKS and input into COMSOL. The inverse-opal structure of this assembly represents the PFSA nanochannels among the IPN nanospheres. The species did not pass through the nanospheres. A 200-nm-thick catalyst layer was introduced at the bottom of the PFSA structure as cathode. A bulk concentration of 0.1 M H^+ was set at the top boundary of the PFSA structure. A constant current density of 200 mA cm^{-2} was applied on the catalyst surface. A free tetrahedral mesh was used with a high element quality optimization. A mesh size of 0.05 to 0.2 μm with a maximum element growth rate of 1.35 and a curvature factor of 0.5 were applied to the geometry. See the Supplementary Methods for more details.

Data availability

All experimental data are available in the main text or the Supplementary Information. Source Data are provided with this paper.

References

1. Whipple, D. T. & Kenis, P. J. A. Prospects of CO_2 utilization via direct heterogeneous electrochemical reduction. *J. Phys. Chem. Lett.* **1**, 3451–3458 (2010).
2. Luna, P. D. et al. What would it take for renewably powered electrosynthesis to displace petrochemical processes? *Science* **364**, eaav3506 (2019).
3. Bushuyev, O. S. et al. What should we make with CO_2 and how can we make it? *Joule* **2**, 825–832 (2018).
4. Jouny, M., Luc, W. & Jiao, F. General eechno-economic analysis of CO_2 electrolysis systems. *Ind. Eng. Chem. Res.* **57**, 2165–2177 (2018).
5. Verma, S., Kim, B., Jhong, H.-R. M., Ma, S. & Kenis, P. J. A. A gross-margin model for defining technoeconomic benchmarks in the electroreduction of CO_2. *ChemSusChem* **9**, 1972–1979 (2016).
6. Zhang, X. et al. Selective and high current CO_2 electro-reduction to multicarbon products in near-neutral KCl electrolytes. *J. Am. Chem. Soc.* **143**, 3245–3255 (2021).
7. Fan, L. et al. Proton sponge promotion of electrochemical CO_2 reduction to multi-carbon products. *Joule* **6**, 205–220 (2022).
8. Liu, W. et al. Electrochemical CO_2 reduction to ethylene by ultrathin CuO nanoplate arrays. *Nat. Commun.* **13**, 1877 (2022).
9. Chen, X. et al. Electrochemical CO_2-to-ethylene conversion on polyamine-incorporated Cu electrodes. *Nat. Catal.* **4**, 20–27 (2021).
10. Arquer, F. P. Gd et al. CO_2 electrolysis to multicarbon products at activities greater than 1 A cm^{-2}. *Science* **367**, 661–666 (2020).
11. Endrődi, B. et al. Operando cathode activation with alkali metal cations for high current density operation of water-fed zero-gap carbon dioxide electrolysers. *Nat. Energy* **6**, 439–448 (2021).
12. Ma, W. et al. Electrocatalytic reduction of CO_2 to ethylene and ethanol through hydrogen-assisted C–C coupling over fluorine-modified copper. *Nat. Catal.* **3**, 478–487 (2020).
13. Yan, Z., Hitt, J. L., Zeng, Z., Hickner, M. A. & Mallouk, T. E. Improving the efficiency of CO_2 electrolysis by using a bipolar membrane with a weak-acid cation exchange layer. *Nat. Chem.* **13**, 33–40 (2021).
14. Xia, C. et al. Continuous production of pure liquid fuel solutions via electrocatalytic CO_2 reduction using solid-electrolyte devices. *Nat. Energy* **4**, 776–785 (2019).
15. Kim, D. et al. Selective CO_2 electrocatalysis at the pseudo-capacitive nanoparticle/ordered-ligand interlayer. *Nat. Energy* **5**, 1032–1042 (2020).
16. Dinh, C.-T. et al. CO_2 electroreduction to ethylene via hydroxide-mediated copper catalysis at an abrupt interface. *Science* **360**, 783–787 (2018).
17. Chen, C., Li, Y. & Yang, P. Address the "alkalinity problem" in CO_2 electrolysis with catalyst design and translation. *Joule* **5**, 737–742 (2021).
18. Rabinowitz, J. A. & Kanan, M. W. The future of low-temperature carbon dioxide electrolysis depends on solving one basic problem. *Nat. Commun.* **11**, 5231 (2020).
19. Huang, J. E. et al. CO_2 electrolysis to multicarbon products in strong acid. *Science* **372**, 1074–1078 (2021).
20. Keith, D. W., Holmes, G., St. Angelo, D. & Heidel, K. A process for capturing CO_2 from the atmosphere. *Joule* **2**, 1573–1594 (2018).
21. Sisler, J. et al. Ethylene electrosynthesis: a comparative techno-economic analysis of alkaline vs membrane electrode assembly vs CO_2–CO–C_2H_4 tandems. *ACS Energy Lett.* **6**, 997–1002 (2021).
22. Greenblatt, J. B., Miller, D. J., Ager, J. W., Houle, F. A. & Sharp, I. D. The technical and energetic challenges of separating (photo) electrochemical carbon dioxide reduction products. *Joule* **2**, 381–420 (2018).
23. Aaron, D. & Tsouris, C. Separation of CO_2 from flue gas: a review. *Sep. Sci. Technol.* **40**, 321–348 (2005).
24. Bondue, C. J., Graf, M., Goyal, A. & Koper, M. T. M. Suppression of hydrogen evolution in acidic electrolytes by electrochemical CO_2 reduction. *J. Am. Chem. Soc.* **143**, 279–285 (2021).
25. Kortlever, R., Balemans, C., Kwon, Y. & Koper, M. T. M. Electrochemical CO_2 reduction to formic acid on a Pd-based formic acid oxidation catalyst. *Catal. Today* **244**, 58–62 (2015).
26. Ooka, H., Figueiredo, M. C. & Koper, M. T. M. Competition between hydrogen evolution and carbon dioxide reduction on copper electrodes in mildly acidic media. *Langmuir* **33**, 9307–9313 (2017).
27. Wu, Y. et al. Electrochemical CO_2 reduction using gas diffusion electrode loading Ni-doped covalent triazine frameworks in acidic electrolytes. *Electrochemistry* **88**, 359–364 (2020).
28. Liu, Z. et al. Acidic electrocatalytic CO_2 reduction using space-confined nanoreactors. *ACS Appl. Mater. Interfaces* **14**, 7900–7908 (2022).
29. Dickinson, E. J. F. & Wain, A. J. The Butler-Volmer equation in electrochemical theory: origins, value, and practical application. *J. Electroanal. Chem.* **872**, 114145 (2020).
30. Noren, D. A. & Hoffman, M. A. Clarifying the Butler–Volmer equation and related approximations for calculating activation losses in solid oxide fuel cell models. *J. Power Sources* **152**, 175–181 (2005).
31. Salvatore, D. & Berlinguette, C. P. Voltage matters when reducing CO_2 in an electrochemical flow cell. *ACS Energy Lett.* **5**, 215–220 (2020).
32. Tao, Z., Pearce, A. J., Mayer, J. M. & Wang, H. Bridge sites of Au surfaces are active for electrocatalytic CO_2 reduction. *J. Am. Chem. Soc.* **144**, 8641–8648 (2022).
33. Gu, J. et al. Modulating electric field distribution by alkali cations for CO_2 electroreduction in strongly acidic medium. *Nat. Catal.* **5**, 268–276 (2022).
34. Monteiro, M. C. O. et al. Absence of CO_2 electroreduction on copper, gold and silver electrodes without metal cations in solution. *Nat. Catal.* **4**, 654–662 (2021).
35. Vennekoetter, J.-B., Sengpiel, R. & Wessling, M. Beyond the catalyst: how electrode and reactor design determine the product spectrum during electrochemical CO_2 reduction. *Chem. Eng. J.* **364**, 89–101 (2019).
36. Kusoglu, A. & Weber, A. Z. New insights into perfluorinated sulfonic-acid ionomers. *Chem. Rev.* **117**, 987–1104 (2017).
37. Yang, F. et al. Investigation of the interaction between Nafion ionomer and surface functionalized carbon black using both ultrasmall angle X-ray scattering and cryo-TEM. *ACS Appl. Mater. Interfaces* **9**, 6530–6538 (2017).
38. Ott, S. et al. Ionomer distribution control in porous carbon-supported catalyst layers for high-power and low Pt-loaded proton exchange membrane fuel cells. *Nat. Mater.* **19**, 77–85 (2020).
39. Lopez-Haro, M. et al. Three-dimensional analysis of Nafion layers in fuel cell electrodes. *Nat. Commun.* **5**, 5229 (2014).
40. Orfanidi, A. et al. The key to high performance low Pt loaded electrodes. *J. Electrochem. Soc.* **164**, F418–F426 (2017).
41. Xu, H., Tao, S. & Jiang, D. Proton conduction in crystalline and porous covalent organic frameworks. *Nat. Mater.* **15**, 722–726 (2016).
42. Lin, S. et al. Covalent organic frameworks comprising cobalt porphyrins for catalytic CO_2 reduction in water. *Science* **349**, 1208–1213 (2015).
43. Wang, H. et al. Organic molecular sieve membranes for chemical separations. *Chem. Soc. Rev.* **50**, 5468–5516 (2021).

44. Resasco, J. et al. Promoter effects of alkali metal cations on the electrochemical reduction of carbon dioxide. *J. Am. Chem. Soc.* **139**, 11277–11287 (2017).
45. Ringe, S. et al. Understanding cation effects in electrochemical CO_2 reduction. *Energy Environ. Sci.* **12**, 3001–3014 (2019).
46. Poojary, S., Islam, M. N., Shrivastava, U. N., Roberts, E. P. L. & Karan, K. Transport and electrochemical interface properties of ionomers in low-Pt loading catalyst layers: effect of ionomer equivalent weight and relative humidity. *Molecules* **25**, 3387 (2020).
47. Sun, R. et al. Periodic evolution of the ionomer/catalyst interfacial structures towards proton conductance and oxygen transport in polymer electrolyte membrane fuel cells. *Nano Energy* **75**, 104919 (2020).
48. Chen, C. et al. Boosting the productivity of electrochemical CO_2 reduction to multi-carbon products by enhancing CO_2 diffusion through a porous organic cage. *Angew. Chem. Int. Ed.* **61**, e202202607 (2022).
49. Tan, Y. C., Lee, K. B., Song, H. & Oh, J. Modulating local CO_2 concentration as a general strategy for enhancing C–C coupling in CO_2 electroreduction. *Joule* **4**, 1104–1120 (2020).
50. O'Brien, C. P. et al. Single pass CO_2 conversion exceeding 85% in the electrosynthesis of multicarbon products via local CO_2 regeneration. *ACS Energy Lett.* **6**, 2952–2959 (2021).
51. Ozden, A. et al. High-rate and efficient ethylene electrosynthesis using a catalyst/promoter/transport layer. *ACS Energy Lett.* **5**, 2811–2818 (2020).
52. Wang, R., Kong, W., Zhou, T., Wang, C. & Guo, J. Organobase modulated synthesis of high-quality β-ketoenamine-linked covalent organic frameworks. *Chem. Commun.* **57**, 331–334 (2021).
53. Bai, L., Gao, Q. & Zhao, Y. Two fully conjugated covalent organic frameworks as anode materials for lithium ion batteries. *J. Mater. Chem. A* **4**, 14106–14110 (2016).
54. Ma, W. et al. Size-controllable synthesis of uniform spherical covalent organic frameworks at room temperature for highly efficient and selective enrichment of hydrophobic peptides. *J. Am. Chem. Soc.* **141**, 18271–18277 (2019).

Acknowledgements

This work was financially supported by the Ontario Research Fund—Research Excellence Program (D.S.), the Natural Sciences and Engineering Research Council (NSERC) of Canada (D.S.), the Australian Research Council through a Discovery Early Career Researcher Award (grant no. DE200100477 to F.L.) and the National Natural Science Foundation of China (grant no. 51603114 to L.H.).

Author contributions

D.S. and F.L. supervised the project. Y.Z. designed and performed all of the electrochemical experiments. L.H. and J.N. synthesized and characterized the COF materials. A.O. prepared PTFE–Cu substrates and fabricated the slim flow-cell. R.K.M. and K.X. designed the permeation flow-cell. R.K.M. and S.Z. performed NMR and ICP analyses. Y.L. performed TEM, zeta potential and contact angle measurements. S.L. and T.A. performed COMSOL modelling. P.O. performed DFT calculations. Y.X., M.F., Y.C., J.E.H. and J.Z. assisted in electrochemical measurements and contributed to data analysis. Y.Z. wrote the manuscript. A.O., C.P.O'.B., F.L., E.H.S. and D.S. contributed to manuscript editing. All of the authors discussed the results and assisted during the manuscript preparation.

Competing interests

The authors declare no competing interests.

Additional information

Supplementary information The online version contains supplementary material available at https://doi.org/10.1038/s44160-022-00234-x.

Correspondence and requests for materials should be addressed to Fengwang Li or David Sinton.

Peer review information *Nature Synthesis* thanks Peng Kang, Anna Klinkova and the other, anonymous, reviewer(s) for their contribution to the peer review of this work. Primary handling editor: Alexandra Groves, in collaboration with the *Nature Synthesis* team.